Test of universal rise of hadronic total cross sections based on πp, Kp and $\bar{p}p$, pp scatterings

Muneyuki Ishida*
Department of Physics, School of Science and Engineering, Meisei University, Hino, Tokyo 191-8506, Japan

Keiji Igi
Theoretical Physics Laboratory, RIKEN, Wako, Saitama 351-0198, Japan
(Received 1 March 2009; published 4 May 2009)

Recently, there have been several evidences that the hadronic total cross section $\sigma_{\rm tot}$ is proportional to $B\log^2 s$, which is consistent with the Froissart unitarity bound. The COMPETE Collaboration has further assumed $\sigma_{\rm tot} \simeq B\log^2(s/s_0) + Z$ to extend its universal rise with the common values of B and s_0 for all hadronic scatterings to reduce the number of adjustable parameters. It was suggested that the coefficient B was universal in the arguments of the color glass condensate of QCD in recent years. However, there has been no rigorous proof yet based only on QCD. We attempt to investigate the value of B for $\pi^{\mp}p$, $K^{\mp}p$ and $\bar{p}p$, pp scatterings, respectively, through the search for the simultaneous best fit to the experimental $\sigma_{\rm tot}$ and ρ ratios at high energies. The $\sigma_{\rm tot}$ at the resonance- and intermediate-energy regions has also been exploited as a duality constraint based on the special form of the finite-energy sum rule. We estimate the values of B, s_0, and Z individually for $\pi^{\mp}p$, $K^{\mp}p$ and $\bar{p}p$, pp scatterings without using the universality hypothesis. It turns out that the values of B are mutually consistent within 1 standard deviation. It has to be stressed that we cannot obtain such a definite conclusion without the duality constraint. It is also interesting to note that the values of Z for πp, Kp, and $\bar{p}(p)p$ approximately satisfy the ratio 2:2:3 predicted by the quark model. The obtained value of B for $\bar{p}(p)p$ is $B_{pp} = 0.280 \pm 0.015$ mb, which predicts $\sigma_{\rm tot}^{pp} = 108.0 \pm 1.9$ mb and $\rho^{pp} = 0.131 \pm 0.0025$ at the LHC energy $\sqrt{s} = 14$ TeV.

DOI: 10.1103/PhysRevD.79.096003 PACS numbers: 11.55.Hx, 13.85.Lg

I. INTRODUCTION

Recently, there have been several evidences [1–6] of the total cross section $\sigma_{\rm tot}$ in the πp and $\bar{p}(p)p$ scatterings, proportional to $\log^2 s$ at high energies, which is consistent with the Froissart unitarity bound [7,8]. The COMPETE Collaboration [2,6] has further assumed $\sigma_{\rm tot} \simeq B\log^2(s/s_0)$ to extend its universal rise with a common value of B for all the hadronic scatterings. The universality of the coefficient B was expected in Ref. [9], and other theoretical support [10,11] based on the arguments describing deep inelastic scattering by gluon saturation in hadron light-cone wave functions (the color glass condensate [12] of QCD) has been given in recent years. However, there is still no rigorous proof based on QCD.

Therefore, it is even worthwhile to prove or disprove this universal rise of $\sigma_{\rm tot}$ empirically. In the near future, the pp total cross section $\sigma_{\rm tot}^{pp}$ in $\sqrt{s} = 14$ TeV will be measured at TOTEM [13] and at another experiment [14] at the LHC. Therefore, the value of B for $\bar{p}p$, pp scattering, B_{pp}, will be determined with good accuracy. On the other hand, the $\pi^- N$ total cross sections $\sigma_{\rm tot}^{\pi^- N}$ have been measured only up to $k = 610$ GeV, where k is the laboratory momentum of π and corresponds to $\sqrt{s} = 33.8$ GeV, as shown by the SELEX Collaboration [15]. Thus, one might doubt that it is possible to obtain the value of B for πp scattering, $B_{\pi p}$, with reasonable accuracy.

In the previous article [5], we attacked this problem by comparing the values of B_{pp} and $B_{\pi p}$ in a new light. We used the laboratory energy of the incident particle, denoted as ν, instead of the center-of-mass energy squared, s. They are related to each other through

$$s = 2M\nu + M^2 + m^2 \tag{1}$$

where M is the mass of the target proton and m is the mass of the incident particle: $m = \mu$ (pion mass), $m = m_K$ (kaon mass), and $m = M$ for πp, Kp, and $\bar{p}(p)p$ scatterings, respectively. The total cross section $\sigma_{\rm tot}$ is composed of the crossing-even cross section $\sigma_{\rm tot}^{(+)}$ and the crossing-odd cross section $\sigma_{\rm tot}^{(-)}$. Its definition will be given in Sec. II. $\sigma_{\rm tot}^{(+)}$ is a sum of a Reggeon component and a non-Reggeon component, and $\sigma_{\rm tot}^{(-)}$ is only made of a Reggeon component corresponding to the vector meson trajectories. The Reggeon components become negligible in the high-energy region. Thus, the $\sigma_{\rm tot}$ at high energies is described only by the non-Reggeon component of $\sigma_{\rm tot}^{(+)}$, which is parametrized by

$$\sigma_{\rm tot}^{(+)} \simeq \frac{4\pi}{m^2}\left(c_2\log^2\frac{\nu}{m} + c_1\log\frac{\nu}{m} + c_0\right). \tag{2}$$

The coefficients c_2, c_1, c_0 are introduced in the respective scatterings.

*ishida@phys.meisei-u.ac.jp

Equation (2) with $c_2 > 0$ shows the shape of a parabola as a function of $\log\nu$ with a minimum. The c_2 parameter controls the rise of the parabola on the high-energy side. We reexpress Eq. (2) as

$$\sigma_{\rm tot}^{(+)} \simeq Z^{ap} + B\log^2\frac{s}{s_0} \tag{3}$$

with $a = \pi^+, K^+, p$. By using the relation $s \simeq 2M\nu$ from Eq. (1) approximated at high energies, the c_2 in Eq. (2) is directly related to the B parameter in Eq. (3). Thus, we obtain the B parameters for the relevant processes individually. In the case of $\bar{p}p$, we have data for large values of $\log\nu$ coming from the Super Proton Synchrotron (SPS) and Tevatron experiments. Thus we can determine the value of $c_2(pp)$ and B_{pp} with good accuracy. On the other hand, in the case of $\pi^- p$, $\pi^+ p$ scatterings, we have used rich information from the experimental $\sigma_{\rm tot}$ data in the low- and intermediate-energy regions through the finite-energy sum rule (FESR). We used the FESR as a constraint between high-energy parameters, and analyzed the $\pi^{\mp}p$ total cross sections $\sigma_{\rm tot}^{\pi^{\mp}p}$ and the ρ ratios $\rho^{\pi^{\mp}p}$, the ratios of real to imaginary parts of the forward scattering amplitudes. Here we adopted the FESR with the integral region between $k = \bar{N}_1$ and $\bar{N}_2$ [16,17]. The k is the laboratory momentum of the incident particle which is related to ν by $k = \sqrt{\nu^2 - m^2}$. $k \simeq \nu$ in high-energy regions. This FESR requires that the low-energy extension of the high-energy asymptotic formula coincides, roughly speaking, with the average of the experimental $\sigma_{\rm tot}$ in the relevant region between $k = \bar{N}_1$ and $\bar{N}_2$. This requirement is called the FESR duality. We have already used [16,17] this sum rule between $\bar{N}_1 = 10$ GeV and $\bar{N}_2 = 20$ GeV. The rich data in $k < 10$ GeV were not included in this case, however. When lower-energy data are included in the integral of $\sigma_{\rm tot}$, one can more precisely determine the subleading term, i.e., the P' term [the term with coefficient $\beta_{P'}$ in Eq. (6) corresponding to $f_2(1275)$ trajectory], which is built in the sense of the FESR [18–20] by the sum of direct-channel resonances. Then, it helps to determine the nonleading term such as $\log\nu$, which then helps to determine the leading term like $\log^2\nu$. Thus, for the πp scatterings, we are able to maximally extend the energy regions of the input data to take $\bar{N}_1 \leq 10$ GeV, so as to obtain the value of $B_{\pi p}$ as accurately as possible.

It is to be noted that the $\bar{p}p$ scattering has open (meson) channels below the $\bar{p}p$ threshold with $\nu < M$ (corresponding to $\sqrt{s} < 2M$), and $\sigma_{\rm tot}^{(+)}$ diverges above the threshold ($\nu > M$) because of the exothermic reactions. The $K^- p$ scattering also has open channels with $\nu < m_K$ (corresponding to $\sqrt{s} < M + m_K$). If we choose the value of $\bar{N}_1$ to be fairly larger than m ($m = M$ for $\bar{p}p$, $m = m_K$ for $K^- p$), we have no difficulty coming from open channels. Contrarily, there are no such effects in πp scattering. Thus, by taking $\bar{N}_1$ as small as possible, we can take into account more resonances through the FESR in order to obtain the low-energy extension from the high-energy side with good accuracy. To obtain a sufficiently small error of $B_{\pi p}$, it appears to be important to include the information from the low-energy scattering data with $0 \leq k \leq 10$ GeV through the FESR.

We will show that the resulting value of $B_{\pi p}$ is consistent [5] with that of B_{pp}, which appears to support the universality hypothesis. It will also be shown that the central value of B_{Kp} is also consistent with B_{pp} and $B_{\pi p}$, although its error is fairly large, due to the present situation of the $K^- p$, $K^+ p$ data. So far, we have searched for the simultaneous best fit of the high-energy parameters such as $c_2, c_1, c_0, \ldots$ to the $\sigma_{\rm tot}$ and the ρ ratios under the duality constraint. In other words, both B (related to c_2) and s_0 (related to c_1/c_2) are completely arbitrary.

We have also attempted to fit data by assuming the universality of B in $\sigma_{\rm tot} \sim B\log^2(s/s_0)$ from the beginning. The fit is successful and the increase of the total fitting χ^2 due to the universality constraint is small. This result also suggests the universality of B. The scale s_0 was assumed to be independent of the colliding particles in Ref. [6]. This resulted in reducing the number of adjustable parameters. But, again, there has been no proof of this assumption based on QCD. We will also investigate this possibility.

In Sec. II, kinematical considerations are summarized for forward $\pi^{\mp}p$, $K^{\mp}p$ and $\bar{p}(p)p$ scatterings. A duality constraint is also explained based on the special form of the FESR. In Sec. III, we explain the approach for how to estimate the value of B, s_0, and Z individually for the above hadron scatterings. In Sec. IV, detailed analyses are given based on $\sigma_{\rm tot}$ and ρ together with the duality constraint. We then discuss the universality of the coefficient B. Section V summarizes our conclusions.

II. KINEMATICAL CONSIDERATIONS

A. Total cross sections $\sigma_{\rm tot}$ and ρ ratios

We take both the crossing-even and crossing-odd forward scattering amplitudes, $F^{(+)}(\nu)$ and $F^{(-)}(\nu)$, defined by

$$\begin{aligned} F^{(\pm)}(\nu) &= \frac{f^{\bar{a}p}(\nu) \pm f^{ap}(\nu)}{2}, \\ f^{\bar{a}p}(\nu) &= F^{(+)}(\nu) + F^{(-)}(\nu), \\ f^{ap}(\nu) &= F^{(+)}(\nu) - F^{(-)}(\nu) \end{aligned} \tag{4}$$

where $(\bar{a}, a) = (\pi^-, \pi^+)$, (K^-, K^+), and $(\bar{p}, p)$ respectively, and $f^{\bar{a}p}(\nu)$, $f^{ap}(\nu)$ are the forward $\bar{a}p$, ap scattering amplitudes. The ν is the incident energy of $\bar{p}(p)$, π, and K in the laboratory system. The combinations (4) of the amplitudes satisfy the crossing property

$$F^{(\pm)}(-\nu) = \pm F^{(\pm)}(\nu)^* \tag{5}$$

under the crossing transformation $\nu \rightarrow -\nu$ for forward amplitudes. We assume that

$$\mathrm{Im}F^{(+)}(\nu) \simeq \frac{\nu}{m^2}\left(c_0 + c_1 \log\frac{\nu}{m} + c_2 \log^2\frac{\nu}{m}\right) + \frac{\beta_{P'}}{m}\left(\frac{\nu}{m}\right)^{\alpha_{P'}}, \tag{6}$$

$$\mathrm{Im}\, F^{(-)}(\nu) \simeq \frac{\beta_V}{m}\left(\frac{\nu}{m}\right)^{\alpha_V}, \tag{7}$$

for $\nu > N$ with some energy N due to the Pomeron-Reggeon exchange model, except for the terms with coefficients c_2 and c_1. The coupling coefficients $\beta_{P'}$, c_0, β_V are the unknown parameters in the Regge theory. $\alpha_{P'}$, α_V are determined phenomenologically. The c_2, c_1 terms are introduced consistently with the Froissart bound to describe the rise of σ_{tot} in the high-energy regions. The total cross sections $\sigma_{\mathrm{tot}}^{\bar{a}p}$, $\sigma_{\mathrm{tot}}^{ap}$ and the ρ ratios $\rho^{\bar{a}p}$ and ρ^{ap} are given by

$$\mathrm{Im}\, f^{\bar{a}p,ap}(\nu) = \frac{k}{4\pi}\sigma_{\mathrm{tot}}^{\bar{a}p,ap}, \qquad \rho^{\bar{a}p} = \frac{\mathrm{Re}f^{\bar{a}p}}{\mathrm{Im}f^{\bar{a}p}}, \qquad \rho^{ap} = \frac{\mathrm{Re}f^{ap}}{\mathrm{Im}f^{ap}}, \tag{8}$$

respectively, where the k are the incident momenta of $\bar{p}(p)$, π, and K in the laboratory system. The total cross section of the crossing-even (odd) part $\sigma_{\mathrm{tot}}^{(\pm)}$ is given by $\sigma_{\mathrm{tot}}^{(\pm)} = (\sigma_{\mathrm{tot}}^{\bar{a}p} \pm \sigma_{\mathrm{tot}}^{ap})/2 = \frac{4\pi}{k}\,\mathrm{Im}F^{(\pm)}(\nu)$. By using the crossing property (5), the real parts are given by [4,17]

$$\mathrm{Re}F^{(+)}(\nu) \simeq \frac{\pi\nu}{2m^2}\left(c_1 + 2c_2 \ln\frac{\nu}{m}\right) - \frac{\beta_{P'}}{m}\left(\frac{\nu}{m}\right)^{\alpha_{P'}} \cot\frac{\pi\alpha_{P'}}{2} + F^{(+)}(0), \tag{9}$$

$$\mathrm{Re}\, F^{(-)}(\nu) \simeq \frac{\beta_V}{m}\left(\frac{\nu}{m}\right)^{\alpha_V} \tan\frac{\pi\alpha_V}{2}, \tag{10}$$

where $F^{(+)}(0)$ is a subtraction constant.

B. Duality constraints

The FESR is used as a duality constraint between these parameters [16,17],

$$\frac{2}{\pi}\int_{N_1}^{N_2}\frac{\nu}{k^2}\,\mathrm{Im}F^{(+)}(\nu)d\nu = \frac{1}{2\pi^2}\int_{\bar{N}_1}^{\bar{N}_2}\sigma_{\mathrm{tot}}^{(+)}(k)dk. \tag{11}$$

The laboratory energy ν is related to the corresponding momentum k by $\nu = \sqrt{k^2 + m^2}$. The momentum corresponding to $\nu = N$ is represented by the quantity with the overline, such as $k = \bar{N}$ in this paper. The $\nu = N_{1,2}$ in Eq. (11) are related to the corresponding momenta $k = \bar{N}_{1,2}$ by $N_{1,2} = \sqrt{\bar{N}_{1,2}^2 + m^2}$. The value of $\bar{N}_2$ should have a reasonably high momentum, above which no resonance structures are observed, while $\bar{N}_1$ may be in the resonance region in the sense of the FESR duality.

The integrand of the left-hand side (LHS) of Eq. (11) is the low-energy extension of Eq. (6). The right-hand side (RHS) is the integral of the experimental $\sigma_{\mathrm{tot}}^{(+)}(= (\sigma_{\mathrm{tot}}^{\bar{a}p} + \sigma_{\mathrm{tot}}^{ap})/2)$ in the resonance-energy regions. This shows several peak and dip structures corresponding to a number of resonances, in addition to the nonresonating background. Thus, Eq. (11) means the FESR duality; that is, the average of these resonance structures plus the nonresonating background in $\sigma_{\mathrm{tot}}^{(+)}$ should coincide with the low-energy extension of the asymptotic formula.

III. THE GENERAL APPROACH

A. Energy region of σ_{tot} and ρ fitted by asymptotic formulas

Let us first discuss the energy regions where experimental σ_{tot} and ρ ratios can be fitted by the asymptotic forms (6)–(10).

As is well known, many low-energy resonances easily join into the smooth high-energy behaviors around the transition energy ν_0. This energy ν_0 is around 5 GeV (which corresponds to $\sqrt{s} \simeq 3.3$ GeV in $\bar{p}p$ scattering) in real experimental data. The value of ν_0 is in the energy region of overlapping resonances and seems to be too small to apply the asymptotic formula to the data just above $\nu = \nu_0$. However, since the average of the low-energy resonances is equivalent to the asymptotic formula due to the FESR duality, we can equate the experimental σ_{tot} to the imaginary part of $F^{(\pm)}(\nu)$ (6) and (7) for $\nu > \nu_0$. Let us now consider the behaviors of the real part of the amplitude. For simplicity of explanation, let us consider the crossing-odd amplitude. Then, we can substitute the RHS of (7) into the principal-part dispersion integral, instead of substituting low-energy resonances, due to the FESR duality. Therefore, we can obtain the RHS of (10) explicitly for $\nu > \nu_0$.

This can easily be extended to the general case. The two-component hypothesis of duality was proposed by Gilman, Harari, and Zarmi [21] for when the scattering amplitude includes the contribution from the Pomeron exchange; i.e., the ordinary Regge pole (P') is built by direct-channel resonances in the sense of the FESR, while the Pomeron-type singularity [which corresponds to Eq. (2) in the present case] is associated with the nonresonating background. If we take this hypothesis, the same argument can be applied, and we can substitute the RHS of (6) into the principal-part dispersion relation from the threshold to obtain the RHS of (9). Therefore, we can use the RHS of (9) for $\nu > \nu_0$. Since the transition energy ν_0 is around 5 GeV as mentioned above, we can use the asymptotic form for both the imaginary part and the real part for $k > 5$ GeV.

B. Practical approach for the search of B

In order to obtain the value of B, we search for the simultaneous best fit to $\sigma_{\mathrm{tot}}^{(+)}$ and the $\rho^{(+)}$ ratios under the duality constraint, Eq. (11). The formulas (4)–(10) and the duality constraint (11) are our starting points. The LHS of Eq. (11) is the integral of the asymptotic formulas (6) and is represented by a linear homogeneous equation of the pa-

rameters $c_{2,1,0}$ and $\beta_{P'}$. The RHS of Eq. (11) is the integral of the experimental $\sigma_{\rm tot}$, which is estimated by using the experimental data of $\sigma_{\rm tot}^{\pi^{\mp}p}$, $\sigma_{\rm tot}^{K^{\mp}p}$, $\sigma_{\rm tot}^{\bar{p}p,pp}$. Here $\bar{N}_2$ is fixed to be 20 GeV, while we take various values of $\bar{N}_1$. We try to take $\bar{N}_1$, being less than 10 GeV, as small as possible. The $\sigma_{\rm tot}^{\bar{a}p,ap}$ and $\rho^{\bar{a}p,ap}$ are fitted simultaneously for the respective processes of πp, Kp and $\bar{p}(p)p$ scatterings. In actual analyses we fit the data of ${\rm Re}f^{\bar{a}p,ap}(k)$ by the formulas (9) and (10). We have obtained them from the experimental data of $\rho^{\bar{a}p,ap}$ in Ref. [6] times ${\rm Im}f_{\rm PDG}^{\bar{a}p,ap}(k)$, where we use the result of the fit given by PDG [6,22]. By using ${\rm Re}f^{\bar{a}p,ap}$ data in the fittings, the resulting χ^2 functions become second-order homogeneous equations of the relevant parameters, which are easy handle. This makes our analyses simple and transparent.

The $\sigma_{\rm tot}^{\bar{a}p,ap}$ for $k \geq 20$ GeV and $\rho^{\bar{a}p,ap}$ for $k \geq 5$ GeV are fitted simultaneously. Here, by considering the transition energy $\nu_0 \sim 5$ GeV, we have chosen $k \geq 5$ GeV for the fitted energy region of the ρ data, while for $\sigma_{\rm tot}$, $k \geq 20$ GeV, which is different from the ρ data. The $\sigma_{\rm tot}$ data up to $k = 20$ GeV are used to obtain their integrals in the duality constraint (11). Thus, in order to avoid the double counting of the data, we use larger values, $k > 20$ GeV, for σ than for ρ.

The high-energy parameters c_2, c_1, c_0, $\beta_{P'}$, and β_V are treated as process dependent, while $\alpha_{P'}$ and α_V are fixed with common values for every process. The duality constraints (11) give constraints between c_2, c_1, c_0 and $\beta_{P'}$ for $\bar{p}(p)p$, Kp and πp scatterings, respectively. $F^{(+)}(0)$ is treated as an additional parameter, and the number of fitting parameters is five for each process. The resulting c_2 are related to the B parameters, defined by $\sigma \simeq B\log^2(s/s_0) + \cdots$, through the equations

$$B_{ap} = \frac{4\pi}{m^2} c_2, \qquad m = M, \mu, m_K, \qquad a = p, \pi, K \tag{12}$$

and we can test the universality of the B parameters.

C. Analysis when the coefficient B and scale s_0 are assumed to be universal

We also analyze the data by assuming the coefficient B of $\sigma_{\rm tot} \sim B\log^2(s/s_0)$ to be universal from the beginning and by testing the universality of B. We also search for the possibility that s_0 has a common value for pp, πp, Kp scatterings.

IV. ANALYSIS BASED ON $\sigma_{\rm tot}$ AND ρ

A. Evaluation of the integral of $\sigma_{\rm tot}^{(+)}$ appearing in the FESR

In order to obtain the explicit forms of the FESR (11), it is necessary to evaluate the integral of $\sigma_{\rm tot}^{(+)}$,

$$\frac{1}{2\pi^2}\int_{\bar{N}_1}^{\bar{N}_2} \sigma_{\rm tot}^{(+)}(k)dk = \frac{1}{2\pi^2}\int_{\bar{N}_1}^{\bar{N}_2} \frac{1}{2}(\sigma_{\rm tot}^{\bar{a}p}(k) + \sigma_{\rm tot}^{ap}(k))dk \tag{13}$$

with $a = \pi^+$, K^+, p from the experimental data [6] for each process. For this purpose we have performed phenomenological fits to the experimental $\sigma_{\rm tot}^{\bar{a}p,ap}$. The experimental $\sigma_{\rm tot}$ can be fitted simply by the phenomenological formula $\sigma_{\rm tot} = \frac{4\pi}{k}\{\frac{\nu}{m^2}(c_2\log^2\frac{\nu}{m} + c_1\log\frac{\nu}{m} + c_0) + \frac{\beta}{m} \times (\frac{\nu}{m})^{0.5} + \frac{d}{m}(\frac{\nu}{m})^{-0.5} + \frac{f}{m}(\frac{\nu}{m})^{-1.5} + \frac{g}{m}(\frac{\nu}{m})^{-2.5}\}$. The dimensionless parameters c_2 are fixed to the values of our previous analysis [16], $c_2 = 0.001\,40$, 0.0185, and 0.0520 for $\pi^{\mp}p$, $K^{\mp}p$, and $\bar{p}(p)p$ scatterings, respectively. The other parameters are taken to be free, depending on the processes. The error of each data point, denoted as Δy, is given by combining the statistical error $\Delta y_{\rm stat}$ and the systematic error $\Delta y_{\rm syst}$ as $\Delta y \equiv \sqrt{(\Delta y_{\rm stat})^2 + (\Delta y_{\rm syst})^2}$. The data of $\sigma_{\rm tot}^{\bar{p}p}$ are mutually inconsistent in the low-energy region among the data of different experiments, and we cannot obtain a good fit. We adopt a statistical method, Sieve algorithm [23], and seven points are removed following this prescription [24]. The experimental $\sigma_{\rm tot}^{\bar{a}p,ap}(k)$ are fitted in the region of laboratory momenta, $k_a < k < 100$ GeV, where k_a are taken to be 3 GeV, 2 GeV, and 2.5 GeV for πp, Kp, and $\bar{p}(p)p$ scatterings, respectively. The k_a correspond to $\sqrt{s} = 2.56$ GeV, 2.35 GeV, and 2.60 GeV for the relevant processes. There are no remarkable resonance structures observed above these energies, and successful fits are obtained by using this simple formula. The g is fixed to be $g = 0$ for the analyses of $\pi^{\mp}p$ and $\bar{p}(p)p$, while it is treated to be free for $K^{\mp}p$. There are five fitting parameters for π^-p, π^+p, $\bar{p}p$, and pp, and six fitting parameters for K^-p and for K^+p. The resulting χ^2 are $\chi^2/(N_D - N_P) = 102.6/(165 - 5)$, $69.7/(100 - 5)$ for π^-p, π^+p; $171.4/(149 - 6)$, $75.0/(86 - 6)$ for K^-p, K^+p; and $48.8/(70 - 5)$, $112.2/(103 - 5)$ for $\bar{p}p$, pp [25].

In the FESR (11) $\bar{N}_2$ is fixed to be $\bar{N}_2 = 20$ GeV, while we take various values of $\bar{N}_1$. The integrals of $\sigma_{\rm tot}^{(+)}(k)$ from the relevant $\bar{N}_1$ to the $\bar{N}_2$ are estimated by using these phenomenological fits.

In πp scatterings, we try to take very small values of $\bar{N}_1$ in the resonance-energy region. There are no open channels below threshold $\nu < \mu$ in this process, and the smaller the $\bar{N}_1$ is taken, the more information in the low-energy region is included through the FESR, and the more accurate value of c_2 is obtained. Actually, we take $\bar{N}_1$ less than 1 GeV. In this case we divide the region of the integral into two parts: The integral of $\sigma_{\rm tot}^{(+)}(k)$ from the higher-energy region, $k_d < k < \bar{N}_2$, is estimated by using the phenomenological fits, while the integral from the lower-energy region, $\bar{N}_1 < k < k_d$, is evaluated directly from experimental data. That is, the data points are connected by straight lines and the areas of these polygonal line graphs are

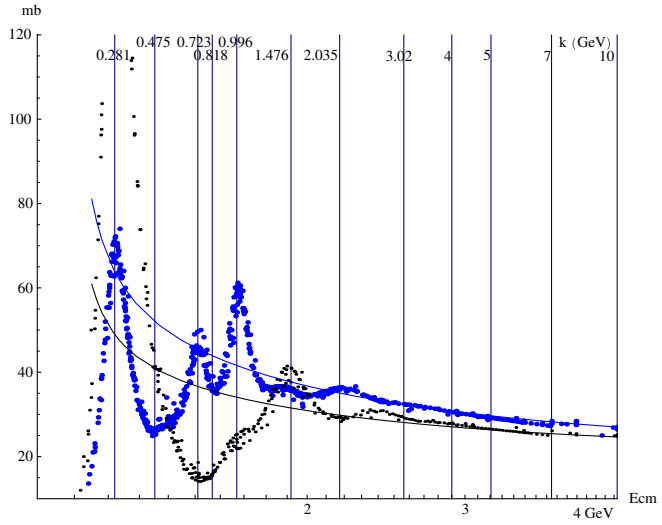

FIG. 1 (color online). The $\sigma_{\rm tot}$ data of $\pi^- p$ scattering (big blue points) and of $\pi^+ p$ scattering (small black points) in the low-energy region: The errors are not shown. The horizontal axis represents the center-of-mass energy $E_{\rm cm}$. The vertical lines correspond to the values of laboratory momenta $k = \bar{N}_1 = 10$, 7, 5, 4, 3.02, 2.035, 1.476, 0.9958, 0.818, 0.723, 0.475, 0.281 GeV, which are selected as the lower limits of the integrals in the FESR (11). Their numbers (in GeV) are shown in the upper part of the figure. The solid lines represent the low-energy extensions of our best fit using the FESR in the case of $\bar{N}_1 = 0.818$ GeV.

regarded as the corresponding integrals. The dividing momentum k_d is taken to be 4 GeV.

The $\sigma_{\rm tot}^{\pi^\mp p}$ data in the low-energy region are shown in Fig. 1. We take $k = \bar{N}_1 = 10$, 7, 5, 4, 3.02, 2.035, 1.476, 0.9958, 0.818, 0.723, 0.475, 0.281 GeV. These values of $\bar{N}_1$, which are shown by vertical lines, correspond to the laboratory momenta of peak and dip positions observed in experimental $\sigma_{\rm tot}^{\pi^\mp p}$ spectra. This can be seen in Fig. 1.

The values of cross-section integrals estimated from the above-mentioned procedures are given in Table I.

The situations are different in $K^\mp p$ and $\bar{p}p$, pp scatterings. $K^- p$ is the exothermic reaction. $K^- p \to \pi^0\Lambda$, $\pi\Sigma$ could occur even at threshold, $\nu = m_K$, and the $\sigma_{\rm tot}^{K^- p}(k)$ increases like $1/k$ near threshold. In the case of too small values of $\bar{N}_1$, the integral of $\sigma_{\rm tot}$ is affected strongly by the contribution from these open channels. Furthermore, in the exotic $K^+ p$ channel there is a sudden decrease of $\sigma_{\rm tot}$ observed below $E_{\rm cm} \simeq 1.9$ GeV ($k \simeq 1.2$ GeV). Similarly, $\bar{p}p$ has a number of open meson channels below threshold, $\nu < M$, and a big dip structure is observed in $\sigma_{\rm tot}$ of the exotic pp channel below $E_{\rm cm} \simeq 2.2$ GeV ($k \simeq 1.4$ GeV). We can see the situations in the $\sigma_{\rm tot}^{K^\mp p}$ and $\sigma_{\rm tot}^{\bar{p}p,pp}$ data shown in Figs. 2 and 3, respectively. The reason for producing these structures is not known, but it is safe to take $\bar{N}_1$ to be fairly larger than m_K and M. Actually, we take $\bar{N}_1 \geq 3$ GeV as $\bar{N}_1 = 10$, 7, 5, 4, 3 GeV in $K^\mp p$ and $\bar{p}p$, pp scatterings. These laboratory momenta are represented by vertical lines in Figs. 2 and 3, respectively.

For each value of $\bar{N}_1$ the integrals of $\sigma_{\rm tot}^{\bar{a}p,ap}$ and their average $\sigma_{\rm tot}^{(+)}$ are estimated by using the phenomenological fits to $K^\mp p$ and $\bar{p}(p)p$ scatterings. The results are given in Tables II and III, respectively.

The values of the integrals given in Tables I, II, and III are estimated with very small errors, which are generally less than 0.3%. We regard central values as exact ones and treat the FESR (11) as exact constraints between the fitting parameters.

B. Analysis of $\pi^\mp p$ scattering

The data [6] of $\sigma_{\rm tot}^{\pi^\mp p}$ for $k \geq 20$ GeV and $\rho^{\pi^\mp p}$ (more exactly, ${\rm Re} f^{\pi^\mp p}$) for $k \geq 5$ GeV are fitted simultaneously. In the FESR (11), $\bar{N}_2$ is taken to be 20 GeV. The $\bar{N}_1$ are chosen to be 10, 7, 5, 4, 3.02, 2.035, 1.476, 0.9958, 0.818, 0.723, 0.475, 0.281 GeV, as explained before.

TABLE I. The integrals of the cross section $\frac{1}{2\pi^2}\int_{\bar{N}_1}^{\bar{N}_2} \sigma_{\rm tot}^{\pi^\mp p}(k)dk$ (GeV^{-1}) and their average, which are estimated by using experimental data for $\pi^\mp p$ scattering: The $\bar{N}_2$ is fixed to be 20 GeV, while we take various values of $\bar{N}_1$.

$\bar{N}_1$–$\bar{N}_2$ (GeV)	$\frac{1}{2\pi^2}\int_{\bar{N}_1}^{\bar{N}_2} \sigma_{\rm tot}^{\pi^- p}(k)dk$	$\frac{1}{2\pi^2}\int_{\bar{N}_1}^{\bar{N}_2} \sigma_{\rm tot}^{\pi^+ p}(k)dk$	$\frac{1}{2\pi^2}\int_{\bar{N}_1}^{\bar{N}_2} \sigma_{\rm tot}^{(+)}(k)dk$
10–20	31.404 ± 0.033	33.611 ± 0.029	32.508 ± 0.022
7–20	41.253 ± 0.042	44.244 ± 0.038	42.748 ± 0.028
5–20	48.069 ± 0.047	51.656 ± 0.044	49.863 ± 0.032
4–20	51.609 ± 0.048	55.536 ± 0.047	53.572 ± 0.034
3.02–20	55.220 ± 0.050	59.539 ± 0.052	57.380 ± 0.036
2.035–20	59.069 ± 0.052	63.899 ± 0.053	61.484 ± 0.037
1.476–20	61.456 ± 0.052	66.443 ± 0.054	63.950 ± 0.038
0.9958–20	63.431 ± 0.053	68.994 ± 0.056	66.213 ± 0.039
0.818–20	63.907 ± 0.053	70.016 ± 0.057	66.961 ± 0.039
0.723–20	64.093 ± 0.053	70.536 ± 0.057	67.314 ± 0.039
0.475–20	64.875 ± 0.053	71.605 ± 0.057	68.240 ± 0.039
0.281–20	67.563 ± 0.054	72.646 ± 0.057	70.105 ± 0.039

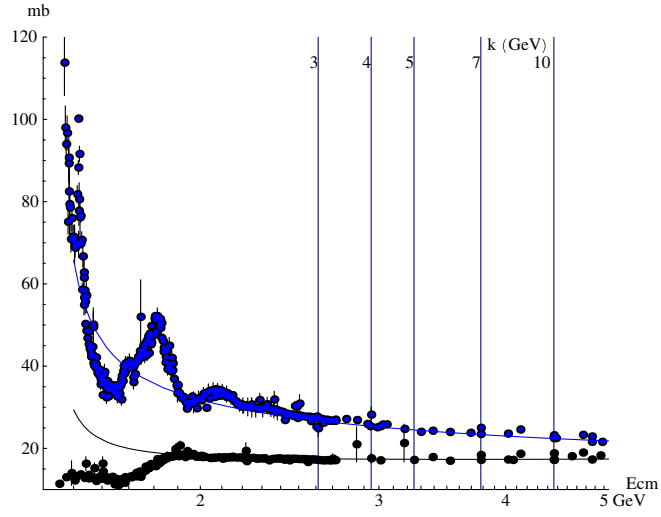

FIG. 2 (color online). The experimental $\sigma_{\rm tot}$ of $K^- p$ (blue points) and of $K^+ p$ (black points) in the low-energy region: The vertical lines correspond to the laboratory momenta $k = \bar{N}_1 = 10, 7, 5, 4, 3$ GeV, which are selected as the lower limits of the FESR integrals (11). Their numbers (in GeV) are shown in the upper part of the figure. The horizontal axis represents the corresponding center-of-mass energy $E_{\rm cm}$. The solid lines represent the low-energy extensions of our best fit using the FESR in the case of $\bar{N}_1 = 5$ GeV.

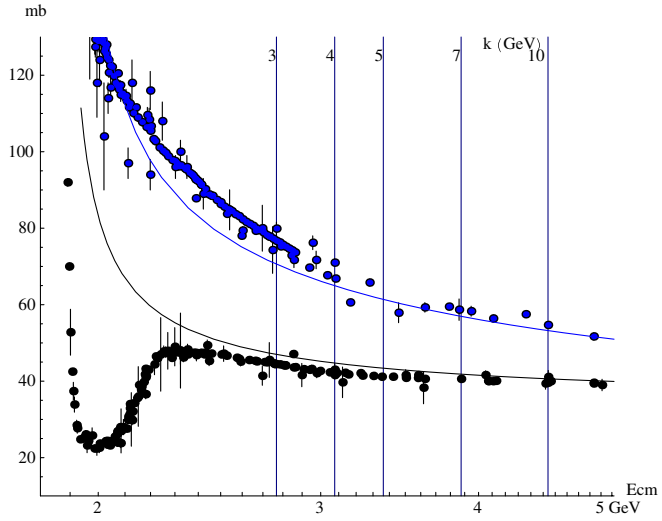

FIG. 3 (color online). The experimental $\sigma_{\rm tot}$ of $\bar{p}p$ (blue points) and of pp (black points) in the low-energy region: The vertical lines correspond to the values of $k = \bar{N}_1$ selected in our analyses. See, the caption in Fig. 2.

For each value of $\bar{N}_1$, the integrals of $\sigma_{\rm tot}^{(+)}$, which are the RHS of Eq. (11), are given in Table I. The integral of the asymptotic formula (6) which appears in the LHS of Eq. (11) is calculable analytically, and we obtain the explicit form of the FESR (11). In the case of $\bar{N}_1 = 0.818$ GeV, for example, the FESR (11) is given by

$$(\pi p) \quad 87.1714\beta_{P'} + 627.26c_0 + 2572.37c_1 + 10\,891.2c_2 = 66.961 \pm 0.039. \tag{14}$$

The error of the RHS is very small, and Eq. (14) is regarded as an exact constraint between the parameters $c_{2,1,0}$ and $\beta_{P'}$. $\beta_{P'}$ is represented by the other three parameters $c_{2,1,0}$ as $\beta_{P'} = \beta_{P'}(c_2, c_1, c_0)$. The fitting is performed with five parameters, including β_V and $F^{(+)}(0)$. The $(\alpha_{P'}, \alpha_V)$ in Eqs. (6) and (7) are fixed to be empirical values (0.500, 0.497) [16] in all the fitting procedures. The values of c_2

TABLE II. The integral of $\sigma_{\rm tot}$ in $K^{\mp} p$: $\frac{1}{2\pi^2}\int_{\bar{N}_1}^{\bar{N}_2} \sigma_{\rm tot}^{K^- p, K^+ p, (+)}(k)dk$ (GeV^{-1}). $\bar{N}_2$ is taken to be 20 GeV, while $\bar{N}_1$ are taken to be 10, 7, 5, 4, 3 GeV, respectively.

$\bar{N}_1$–$\bar{N}_2$ (GeV)	$\frac{1}{2\pi^2}\int_{\bar{N}_1}^{\bar{N}_2} \sigma_{\rm tot}^{K^- p}(k)dk$	$\frac{1}{2\pi^2}\int_{\bar{N}_1}^{\bar{N}_2} \sigma_{\rm tot}^{K^+ p}(k)dk$	$\frac{1}{2\pi^2}\int_{\bar{N}_1}^{\bar{N}_2} \sigma_{\rm tot}^{(+)}(k)dk$
10–20	28.217 ± 0.068	22.661 ± 0.053	25.439 ± 0.043
7–20	37.175 ± 0.094	29.377 ± 0.069	33.276 ± 0.058
5–20	43.425 ± 0.110	33.818 ± 0.077	38.622 ± 0.067
4–20	46.693 ± 0.116	36.031 ± 0.080	41.362 ± 0.070
3–20	50.120 ± 0.120	38.257 ± 0.081	44.189 ± 0.072

TABLE III. The integral of $\sigma_{\rm tot}$ in $\bar{p}p$, pp: $\frac{1}{2\pi^2}\int_{\bar{N}_1}^{\bar{N}_2} \sigma_{\rm tot}^{\bar{p}p, pp, (+)}(k)dk$ (GeV^{-1}). $\bar{N}_2$ is taken to be 20 GeV, while $\bar{N}_1$ is taken to be 10, 7, 5, 4, 3 GeV.

$\bar{N}_1$–$\bar{N}_2$ (GeV)	$\frac{1}{2\pi^2}\int_{\bar{N}_1}^{\bar{N}_2} \sigma_{\rm tot}^{\bar{p}p}(k)dk$	$\frac{1}{2\pi^2}\int_{\bar{N}_1}^{\bar{N}_2} \sigma_{\rm tot}^{pp}(k)dk$	$\frac{1}{2\pi^2}\int_{\bar{N}_1}^{\bar{N}_2} \sigma_{\rm tot}^{(+)}(k)dk$
10–20	65.75 ± 0.24	51.07 ± 0.06	58.41 ± 0.12
7–20	87.61 ± 0.33	66.68 ± 0.07	77.14 ± 0.17
5–20	103.48 ± 0.39	77.28 ± 0.08	90.38 ± 0.20
4–20	112.11 ± 0.41	82.72 ± 0.08	97.41 ± 0.21
3–20	121.51 ± 0.41	88.33 ± 0.08	104.92 ± 0.21

TABLE IV. Values of c_2 from πp scattering in the best fit with five parameters, using the FESR as a constraint. The fittings χ^2 are given in the next row. The number of data points is 162. The result of the six-parameter fit without using the FESR is also shown in the last column as "No SR."

$\bar{N}_1$	10	7	5	4	3.02	2.035	1.476
$c_2(10^{-5})$	142(21)	136(19)	132(18)	129(17)	124(16)	117(15)	116(14)
$\chi^2_{\rm tot}$	149.05	149.35	149.65	149.93	150.44	151.25	151.38
$\bar{N}_1$	0.9958	0.818	0.723	0.475	0.281		No SR
$c_2(10^{-5})$	116(14)	121(13)	126(13)	140(13)	121(12)		164(29)
$\chi^2_{\rm tot}$	151.30	150.51	149.90	148.61	150.39		147.78

and χ^2 in the best fits for the respective $\bar{N}_1$ are given in Table IV [26].

As is seen in Table IV, values of the best-fitted c_2 are almost independent of the choices of $\bar{N}_1$ (except for the case $\bar{N}_1 = 0.475$ GeV). The results are surprisingly stable, although there are many resonant structures and $\sigma_{\rm tot}^{\pi^{\mp}p}$ show sharp peak and dip structures in this energy region.

We can adopt the case of $\bar{N}_1 = 0.818$ GeV as a representative of our results. The best-fit value of c_2 is

$$c_2 = (121 \pm 13) \times 10^{-5}. \tag{15}$$

The best-fit values of the other parameters are given in Table V.

The result should be compared to the analysis without the FESR. In this case there is no constraint between parameters, and the fitting is performed with six parameters including $\beta_{P'}$. The best-fit value of c_2 is

$$c_2 = (164 \pm 29) \times 10^{-5}. \tag{16}$$

This value should be compared with the result (15) using the FESR. By including rich information of low-energy scattering data in the form of the FESR, the error of c_2 in Eq. (15) becomes less than half of Eq. (16).

Predicted spectra of $\sigma_{\rm tot}$ without the FESR are shown in Fig. 4 and with the FESR in Fig. 5. The uncertainties of the prediction from the best fit are shown by the shaded regions in Figs. 4 and 5, which correspond to c_2 in Eqs. (16) and (15), respectively. Our prediction in Fig. 5 is greatly improved from that in Fig. 4.

The results of the fit to $\rho^{\pi^{\mp}p}$ are given in Fig. 6.

TABLE V. Values of the best-fitted parameters and their 1 standard deviations in $\pi^{\mp}p$ scattering. The FESR with $\bar{N}_1 = 0.818$ GeV is used, and $\beta_{P'}$ is obtained from the other parameters by using this FESR. Our predicted lines in Fig. 5 are depicted by using these values.

$c_2(10^{-5})$	c_1	c_0	$F^{(+)}(0)$	β_V	$\beta_{P'}$
121.1	−0.011 79	0.1141	−0.0180	0.040 04	0.1437
+13.3	−0.013 85	0.1224	−0.2785	0.039 91	0.1280
−13.3	−0.009 74	0.1058	0.2425	0.040 18	0.1594

The $c_2 \log^2 \frac{\nu}{\mu} + c_1 \log \frac{\nu}{\mu}$ with $c_2 > 0$ shows the shape of the parabola as a function of $\log \frac{\nu}{\mu}$ with a minimum. In order to determine the c_2, c_1 coefficients of $\log^2 \frac{\nu}{\mu}$ and $\log \frac{\nu}{\mu}$ with sufficient accuracy, a few orders of magnitude are necessary for the fitted energy region. The fitted energy region for $\pi^- p$ is 20 GeV $< k <$ 370 GeV, shown by the horizontal arrow in the figure, which corresponds to 6.2 GeV $< E_{\rm cm} (\equiv \sqrt{s}) <$ 26.4 GeV. This energy range is insufficient to determine c_2 with enough accuracy.

The energy region of the FESR integral, $\bar{N}_1 (= 0.818$ GeV$) < k <$ 20 GeV (which corresponds to $1.56 < \sqrt{s} = E_{\rm cm} <$ 6.2 GeV) is shown by the double horizontal arrow in Fig. 5. Additional information from this energy region greatly helps to improve our estimate of c_2. It is very important to include the information of the data in the low-energy region by using the FESR.

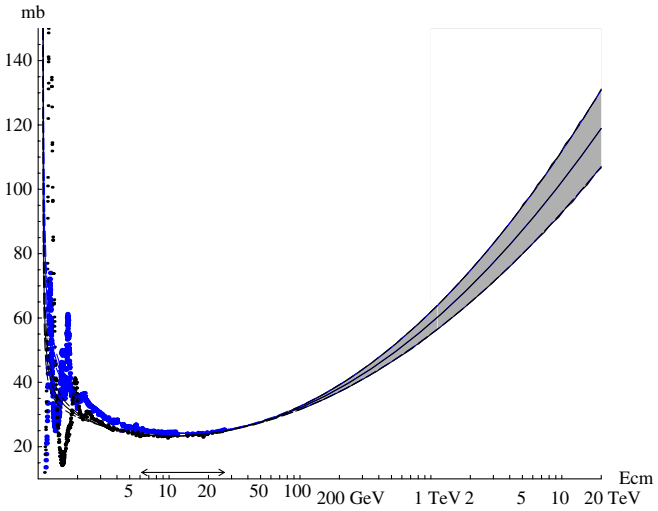

FIG. 4 (color online). Prediction of $\sigma_{\rm tot}^{\pi p}$ without the FESR. The data points are given with no error bars. The big blue points (line) are data (best-fitted curve) for $\pi^- p$. The black points and lines are for $\pi^+ p$. The horizontal arrow represents the energy region of the fitting. The shaded region corresponds to the uncertainty of the prediction by the best fit, where $c_2 = (164 \pm 29) \times 10^{-5}$. The c_2 has large uncertainties since it is not determined well by direct fitting of the data above $k = 20$ GeV ($E_{\rm cm} = 6.2$ GeV).

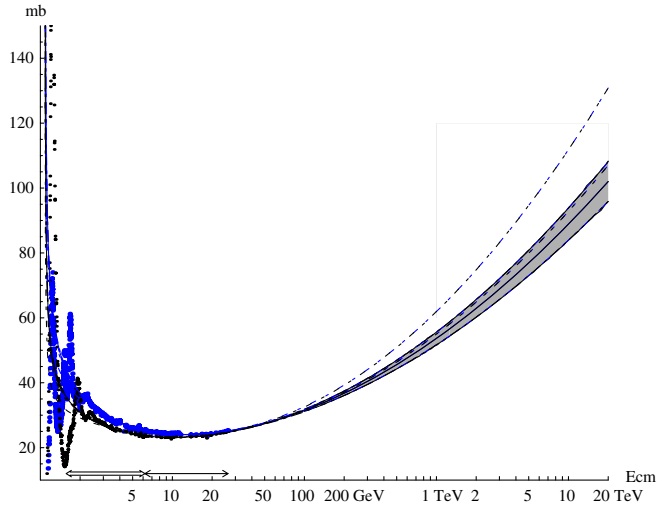

FIG. 5 (color online). Prediction of $\sigma_{\rm tot}^{\pi p}$ with the use of the FESR in the case of $\bar{N}_1 = 0.818$ GeV as a constraint. The data points are given with no error bars. The big blue points (line) are data (best-fitted curve) for $\pi^- p$. The black points and lines are for $\pi^+ p$. The single horizontal arrow represents the energy region of the fitting, while the double horizontal arrow represents the energy region of the FESR integral, $k = \bar{N}_1$ through $\bar{N}_2$ (= 20 GeV). The uncertainty of the prediction by the best fit is shown by the shaded region, where $c_2 = (121 \pm 13) \times 10^{-5}$. It is greatly improved from that without the FESR, shown by the dashed line. The inclusion of rich information of low-energy scattering data through the FESR is essential to determine c_2.

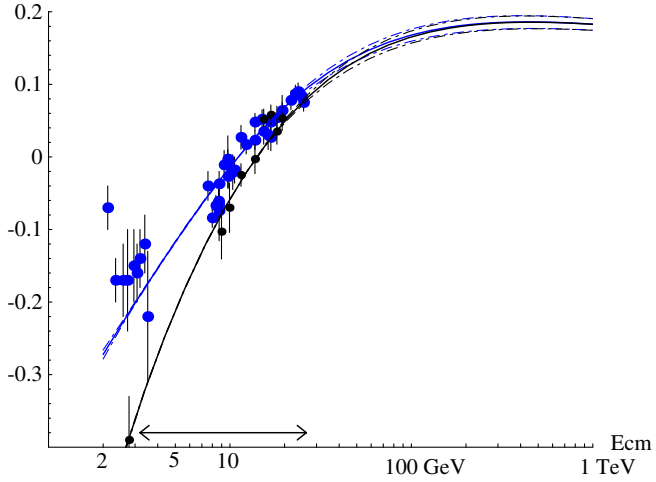

FIG. 6 (color online). Result of the fit and the prediction of $\rho^{\pi^\mp p}$ with the use of the FESR in the case of $\bar{N}_1 = 0.818$ GeV as a constraint. The big blue points (line) are data (best-fitted curve) for $\pi^- p$. The black points and lines are for $\pi^+ p$. The horizontal arrow represents the energy region of the fitting.

The value of $\sigma_{\rm tot}$ in $\pi^- N$ scattering at $k = 610$ GeV ($E_{\rm cm} = 33.8$ GeV) is reported by the SELEX Collaboration [15] as $\sigma_{\rm tot}^{\pi N} = 26.6 \pm 0.9$ mb. Here N is not identified with a proton or a neutron. Our prediction of $\sigma_{\rm tot}^{(+)}$ [$= (\sigma_{\rm tot}^{\pi^- p} + \sigma_{\rm tot}^{\pi^+ p})/2$] at this energy is 25.75 ± 0.05 mb, and $\sigma_{\rm tot}^{\pi^- p} - \sigma_{\rm tot}^{\pi^+ p}$ is 0.30 mb. By taking this value into account we may predict $\sigma_{\rm tot}^{\pi^- N} = 25.8 \pm 0.3$ mb at $k = 610$ GeV. This is consistent with the SELEX measurement.

In Fig. 1, our best-fitted curve in the case of $\bar{N}_1 = 0.818$ GeV is also depicted. The fitted energy region is above $k = 20$ GeV ($E_{\rm cm} = 6.2$ GeV), and it is far above the energy region shown in Fig. 1. Nevertheless, the low-energy extensions of the asymptotic formula almost coincide with the experimental $\sigma_{\rm tot}^{\pi^\mp p}$ in $E_{\rm cm}$ up to $\sim$3 GeV, and in $E_{\rm cm} < \sim$3 GeV they seem to cross the averages of peak and dip structures of various N and Δ resonances. This shows that the FESR duality is satisfied in our best fit.

C. Analysis of $K^\mp p$ scattering

The $K^- p$ and $K^+ p$ scatterings are analyzed using the same method. We fix $\bar{N}_2 = 20$ GeV, while we take various values of $\bar{N}_1$ as $\bar{N}_1 = 10$, 7, 5, 4, 3 GeV. The integral of $\sigma_{\rm tot}^{(+)}$ [$= (\sigma_{\rm tot}^{K^- p} + \sigma_{\rm tot}^{K^+ p})/2$] for each value of $\bar{N}_1$ is given in Table II, and the FESR (11) is written in an explicit form. In the case of $\bar{N}_1 = 5$ GeV, the FESR is given by

$$(Kp) \qquad 8.213\,63\beta_{P'} + 39.2291 c_0 + 124.142 c_1 + 398.549 c_2 = 38.62 \pm 0.07, \tag{17}$$

which is regarded as a constraint between parameters $c_{2,1,0}$ and $\beta_{P'}$. Solving this constraint, $\beta_{P'}$ is represented by the other three parameters. The experimental $\sigma_{\rm tot}^{K^\mp p}$ in $k \geq 20$ GeV and $\rho^{K^\mp p}$ (more exactly, ${\rm Re} f^{K^\mp p}$) in $k \geq 5$ GeV are fitted simultaneously with five parameters, $c_{2,1,0}$, β_V, and $F^{(+)}(0)$, where $\alpha_{P'}$, α_V are fixed with values common to the πp case, $\alpha_{P'} = 0.5$, $\alpha_V = 0.497$. The fits are successful, independently of the choices of $\bar{N}_1$, as shown in Table VI, where we only show the values of c_2 and the total χ^2 in the best fits.

TABLE VI. Values of c_2 and χ^2 in the best fits to $\sigma_{\rm tot}^{K^\mp p}$ and $\rho^{K^\mp p}$. The FESR with the integrals $\bar{N}_1$ through $\bar{N}_2$ are used as constraints. $\bar{N}_2$ is fixed to 20 GeV, while we take various values of $\bar{N}_1$. The number of data points is 111, fitted with five parameters in the case with the FESR. The result with no FESR is given in the last column as "No SR."

$\bar{N}_1$ (GeV)	10	7	5	4	3	No SR
$c_2(10^{-4})$	179(61)	176(54)	176(49)	176(47)	174(44)	266(95)
$\chi^2_{\rm tot}$	64.01	63.90	63.80	63.76	63.77	62.29

TABLE VII. Values of the best-fitted parameters and their 1 standard deviations in $K^{\mp}p$ scattering. The FESR with $\bar{N}_1 = 5$ GeV is used, and $\beta_{P'}$ is obtained from the other parameters by using this FESR. Our predicted lines in Fig. 8 are depicted by using these values.

$c_2(10^{-4})$	c_1	c_0	$F^{(+)}(0)$	β_V	$\beta_{P'}$
175.7	−0.1388	1.207	1.660	0.5684	0.1840
+49.5	−0.2042	1.439	0.640	0.5668	−0.1775
−49.5	−0.0733	0.974	2.680	0.5699	0.5455

The central values of c_2 in the best fits are very stable, and almost independent of the choices of $\bar{N}_1$. We choose $\bar{N}_1 = 5$ GeV as a representative of our results. This value is fairly larger than the momentum of the dip structure observed in $\sigma_{\rm tot}^{K^+p}$ below $k \simeq 1.2$ GeV. The best-fitted value of c_2 is

$$c_2 = (176 \pm 49) \times 10^{-4}. \tag{18}$$

The values of the other parameters are given in Table VII. The results are compared with the analysis without the FESR,

$$c_2 = (266 \pm 95) \times 10^{-4}. \tag{19}$$

This uncertainty of c_2 is very large, since the range of momenta of the fitting 20 GeV $< k <$ 310 GeV, which corresponds to 6.2 GeV $< E_{\rm cm} <$ 24.1 GeV, is insufficient to determine c_2 accurately by direct fitting. The best-fit value of $\beta_{P'}$ becomes negative and unphysical. Thus, the central value $c_2 = 266 \times 10^{-4}$ is considered to be too large and unreliable.

By including the data above $k = 5$ GeV ($E_{\rm cm} = 3.25$ GeV) in the form of the FESR, the error of c_2 in

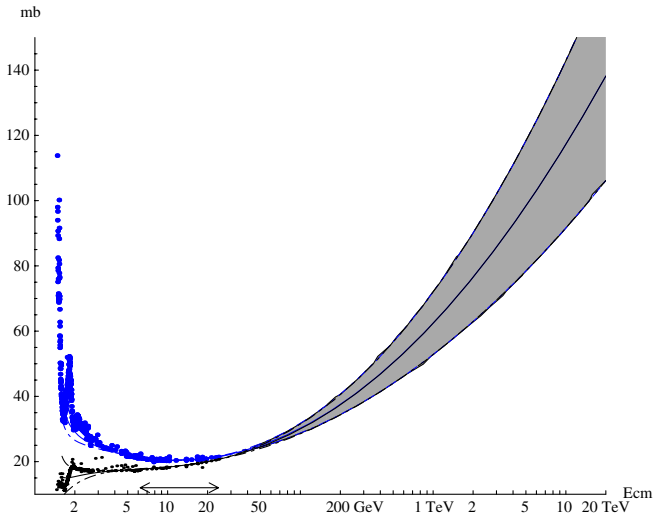

FIG. 7 (color online). Prediction of $\sigma_{\rm tot}^{Kp}$ without the FESR. The data points are given with no error bars. The big blue points (line) are data (best-fitted curve) for K^-p. The black points and lines are for K^+p. The horizontal arrow represents the energy region of the fitted data. The shaded region represents the uncertainty of the prediction, where $c_2 = (266 \pm 95) \times 10^{-4}$. The c_2 has a very large uncertainty since it is not determined well by directly fitting to the high-energy experimental data.

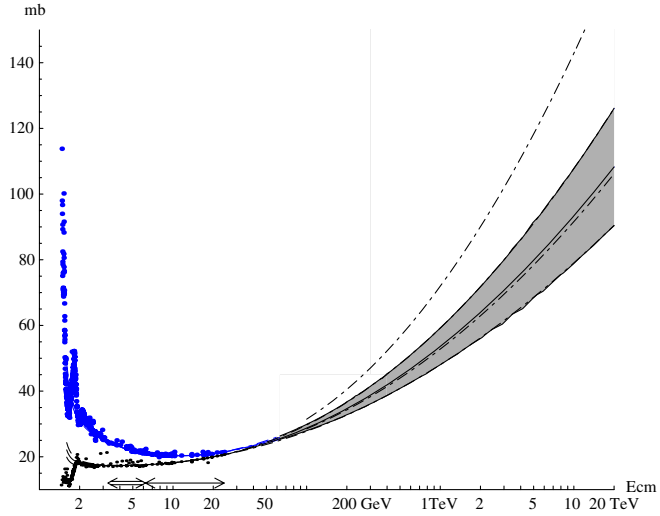

FIG. 8 (color online). Prediction of $\sigma_{\rm tot}^{Kp}$ with the FESR in the case of $\bar{N}_1 = 5$ GeV as a constraint: The big blue points (line) are data (best-fitted curve) for K^-p. The black points and lines are for K^+p. The single horizontal arrow represents the energy region of the fitted data, while the double horizontal arrow represents the energy region of the FESR integral, $k = \bar{N}_1$ through $\bar{N}_2$ (= 20 GeV). The data points are given with no error bars. The uncertainty of the prediction by the best fit, shown by the shaded region, is improved from that without the FESR, represented by the dot-dashed line. The best-fitted c_2 is $c_2 = (176 \pm 49) \times 10^{-4}$. The inclusion of the information of low-energy data by the FESR is essential to improve the estimation of c_2.

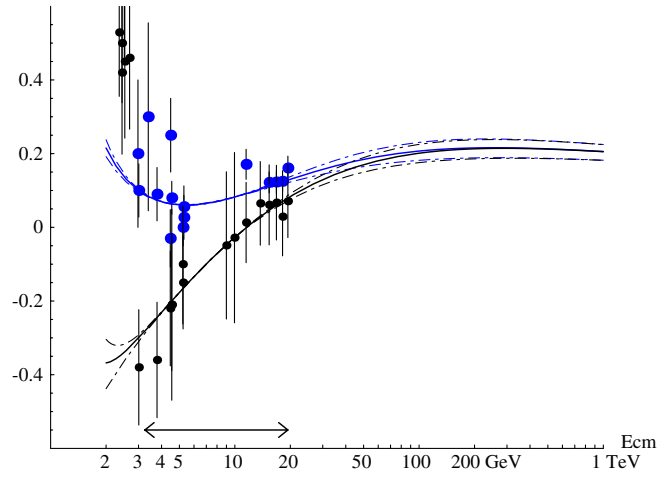

FIG. 9 (color online). Result of the fit and the prediction of $\rho^{K^{\mp}p}$ with the use of the FESR in the case of $\bar{N}_1 = 5$ GeV as a constraint. The big blue points (line) are data (best-fitted curve) for K^-p. The black points and lines are for K^+p. A horizontal arrow represents the energy region of the fitting.

TABLE VIII. Values of c_2 and the total χ^2 in the best fit to $\bar{p}p$, pp scatterings, using the FESR as a constraint. The data up to the Tevatron energy, $E_{\rm cm} = 1.8$ TeV, are fitted simultaneously. The number of data points is 234, fitted by five parameters when using the FESR as a constraint. The result of the six-parameter fit without using the FESR is also shown in the last column as "No SR."

$\bar{N}_1$	10	7	5	4	3	No SR
$c_2(10^{-4})$	505(28)	506(27)	504(26)	500(26)	493(25)	491(34)
$\chi^2_{\rm tot}$	214.52	214.53	214.32	214.14	213.99	213.98

Eq. (18) becomes about half of Eq. (19). Correspondingly, the predicted spectra with the FESR given in Fig. 8 are greatly improved from Fig. 7 without the FESR. The inclusion of the information in the low-energy region is essential to determine the value of c_2 reliably in Kp scattering. The fitting result and prediction of ρ^{K^-p,K^+p} using FESR are given in Fig. 9.

Figure 2 shows the data in the low-energy region. The low-energy extensions of our best-fitted curves in the case of $\bar{N}_1 = 5$ GeV are also depicted in this figure. They reproduce surprisingly well the experimental $\sigma_{\rm tot}^{K^-p}$ and $\sigma_{\rm tot}^{K^+p}$, although the energy region of the FESR integral and the energy region of the fitting are above the energy region shown in this figure. This shows that our best-fitted curves satisfy the FESR duality.

D. Analysis of $\bar{p}p$, pp scatterings

Similarly to the Kp scatterings, in the analysis of $\bar{p}p$, pp scatterings we fix $\bar{N}_2 = 20$ GeV, while we take various values of $\bar{N}_1$ as $\bar{N}_1 = 10, 7, 5, 4, 3$ GeV. For each value of $\bar{N}_1$, the FESR (11) is written in an explicit form, where the integral of $\sigma_{\rm tot}^{(+)}$ [$= (\sigma_{\rm tot}^{\bar{p}p} + \sigma_{\rm tot}^{pp})/2$] is given in Table III. In the case of $\bar{N}_1 = 5$ GeV, for example, the FESR is given by

$$(pp) \quad 3.140\,58\beta_{P'} + 10.8947c_0 + 27.5046c_1 + 71.0017c_2 = 90.38 \pm 0.20, \tag{20}$$

which is regarded as a constraint between parameters $c_{2,1,0}$ and $\beta_{P'}$, and leads to the relation $\beta_{P'} = \beta_{P'}(c_2, c_1, c_0)$.

The $\sigma_{\rm tot}^{\bar{p}p}$ data are obtained up to $E_{\rm cm} = 63$ GeV by the Intersecting Storage Ring Accelerator (ISR) experiment, up to $E_{\rm cm} = 0.9$ TeV by the SPS experiment, and up to $E_{\rm cm} = 1.8$ TeV by the Tevatron experiment. There are two conflicting measurements in the Tevatron experiment, which are from D0 [27,28] and CDF [29]. The very high-energy data with large uncertainties are obtained by cosmic ray experiments.

TABLE IX. Values of the best-fitted parameters and their 1 standard deviations in $\bar{p}p$, pp scattering. The FESR with $\bar{N}_1 = 5$ GeV is used, and $\beta_{P'}$ is obtained from the other parameters by using this FESR. Our predicted lines in Figs. 10 and 11 are depicted by using these values.

$c_2(10^{-4})$	c_1	c_0	$F^{(+)}(0)$	β_V	$\beta_{P'}$
503.6	−0.2432	6.647	10.51	3.721	6.713
+26.1	−0.2810	6.788	10.24	3.728	6.495
−26.1	−0.2054	6.505	10.77	3.714	6.931

The experimental $\sigma_{\rm tot}^{\bar{p}p,pp}$ in $k \geq 20$ GeV and $\rho^{\bar{p}p,pp}$ in $k \geq 5$ GeV, up to Tevatron energy, are fitted simultaneously. The fittings are performed with five parameters, $c_{2,1,0}$, β_V, and $F^{(+)}(0)$, by using the FESR as a constraint [30]. The best-fitted values of c_2 and total χ^2 for the respective values of $\bar{N}_1$ are given in Table VIII. The result is compared with the six-parameter fit of the analysis without using the FESR, denoted as "No SR" in the same table. By considering this result, we choose $\bar{N}_1 = 5$ GeV as a representative of our analyses. The best-fitted c_2 is given by

$$c_2 = (504 \pm 26) \times 10^{-4}. \tag{21}$$

The values of the other parameters are given in Table IX.

The improvement from the result $c_2 = (491 \pm 34) \times 10^{-4}$ obtained by the fit without using the FESR is not large, since the high-energy data from the SPS and Tevatron experiments, which directly affect the estimation of the c_2 value, are included in both fits.

Our predicted spectra of $\sigma_{\rm tot}^{\bar{p}p,pp}$ in the case of $\bar{N}_1 = 5$ GeV are given in Fig. 10. The fitting result and prediction of $\rho^{\bar{p}p,pp}$ are given in Fig. 11.

E. Test of the universality of B

Using the values of the parameters given in the previous subsections, we can test the universality of the B parameters from the experimental data of $\pi^{\mp}p$, $K^{\mp}p$ and $\bar{p}(p)p$ scatterings.

In Ref. [6] the asymptotic formula of the total cross section is represented in terms of squared center-of-mass energy s in the form

$$\sigma_{\rm tot}^{(+)} \simeq Z^{ap} + B\log^2\frac{s}{s_0}, \tag{22}$$

which is already given in Eq. (3). In Ref. [6] B and s_0 are assumed to be universal in the relevant processes while Z_{ap} are taken to be process dependent [33].

We use the asymptotic formula of the crossing-even amplitude (6), which gives

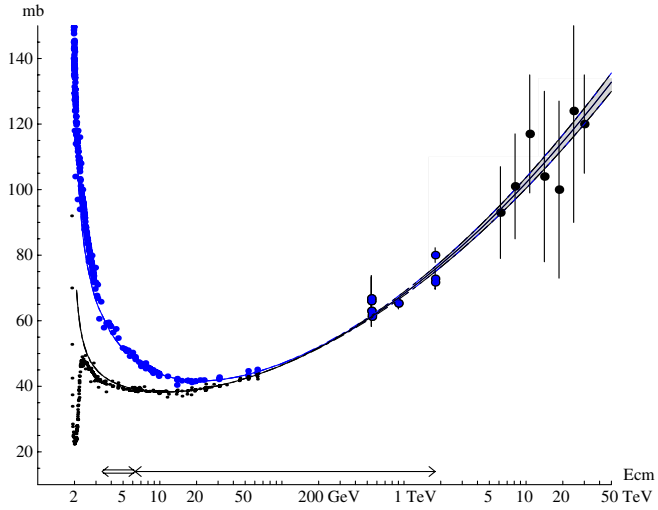

FIG. 10 (color online). Prediction of $\sigma_{\rm tot}^{\bar{p}p,pp}$ with the FESR: The data up to the Tevatron energy are fitted simultaneously. The single horizontal arrow represents the energy region of the fitting. The big blue points (line) are data (best-fitted curve) for $\bar{p}p$. The black points and lines are for pp. The data points are given with no error bars. The double horizontal arrow represents the energy region of the FESR integral, $k = \bar{N}_1$ (= 5 GeV in this case) through $\bar{N}_2$ (= 20 GeV). The shaded region corresponds to the uncertainty of our prediction in the best fit, where $c_2 = (504 \pm 26) \times 10^{-4}$.

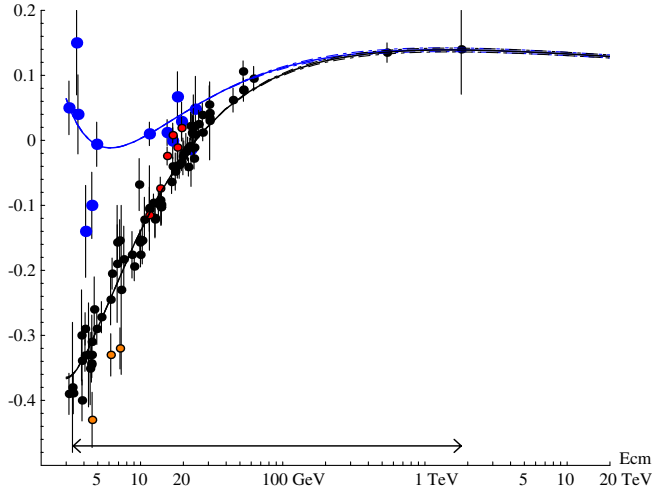

FIG. 11 (color online). Result of the fit and the prediction of $\rho^{\bar{p}p,pp}$ with the use of the FESR in the case of $\bar{N}_1 = 5$ GeV as a constraint. The big blue points (line) are data (best-fitted curve) for $\bar{p}p$. The black points and lines are for pp. The horizontal arrow represents the energy region of the fitting. The ρ^{pp} data from Ref. [31] [six (red) points around $\rho^{pp} \simeq 0.0$] and from Ref. [32] [three (orange) points around $\rho^{pp} \simeq -0.3$] are removed from our best fit.

$$\sigma_{\rm tot}^{(+)} \simeq \frac{4\pi}{m^2}\left(c_0 + c_1 \log\frac{\nu}{m} + c_2 \log^2\frac{\nu}{m}\right). \tag{23}$$

It is the same equation as Eq. (2). Here we omit the P' term proportional to $\beta_{P'}$ and use the approximation $\nu/k \simeq 1$ at high energies.

Using the relation $s \simeq 2M\nu$ at high energies from Eq. (1), we obtain the relation between the parameters,

$$B = \frac{4\pi}{m^2} c_2, \tag{24}$$

$$Z^{ap} = \frac{4\pi}{m^2}\left(c_0 - \frac{{c_1}^2}{4c_2}\right), \tag{25}$$

$$s_0 = 2Mm \exp\left[-\frac{c_1}{2c_2}\right] + M^2 + m^2. \tag{26}$$

The parameters $c_{2,1,0}$ are treated as process dependent in our analyses. Substituting the best-fitted values of $c_{2,1,0}$ into these equations, we can estimate the values of B, Z^{ap}, $\sqrt{s_0}$ individually for πp, Kp and $\bar{p}p$, pp scatterings without using the universality hypothesis. The results are given in Table X.

The results with the FESR are given in the LHS, and those without the FESR are given in the RHS.

As shown in this table, in the case using the FESR, the values of B for πp, Kp and $\bar{p}(p)p$ scatterings, denoted, respectively, as $B_{\pi p}$, B_{Kp} and B_{pp}, are mutually consistent within 1 standard deviation.

In contrast, if we do not use the FESR as constraints, $B_{\pi p}$ and B_{Kp} have large uncertainties, and we cannot obtain any definite conclusion.

It is very interesting that by including rich information of low-energy scattering data through the FESR, the central values of B become mutually closer, and consistent with each other. The FESR duality suggests the universality of B.

Another interesting feature is the value of Z^{ap}. If we neglect relatively small contributions from the $\beta_{P'}$ and β_V terms, the Z^{ap} are equal to the $\sigma_{\rm tot}$ at energy $\sqrt{s_0}$, which is

TABLE X. Values of B, Z^{ap}, and $\sqrt{s_0}$ obtained from our best fits with the FESR (LHS) and without the FESR (RHS). The B, Z^{ap}, and $\sqrt{s_0}$ are estimated individually for the processes of πp, Kp, and $\bar{p}(p)p$ scatterings.

	B (mb)	Z^{ap} (mb)	$\sqrt{s_0}$ (GeV)	B (mb)	Z^{ap} (mb)	$\sqrt{s_0}$ (GeV)
πp	0.304(34)	21.45(32)	5.92(90)	0.411(73)	22.99	9.71
Kp	0.354(99)	18.7(1.1)	7.1(2.6)	0.535(190)	20.67	12.14
$\bar{p}(p)p$	0.280(15)	35.31(36)	4.63(53)	0.273(19)	34.98	4.28

the lowest point of the parabola (23) of $\log\frac{\nu}{m}$. The values of Z^{ap} for πp, Kp and $\bar{p}(p)p$ approximately satisfy the relation of the quark model, $Z^{\pi p}:Z^{Kp}:Z^{pp} \simeq 2:2:3$. Z^{ap} and the parameters $\beta_{P'}$ and β_V appearing in the Regge theory are controlled by nonperturbative soft physics of QCD, while the term $B\log^2 s/s_0$ describing the rise of $\sigma_{\rm tot}$ is plausibly universal for hadron-hadron scatterings.

It is to be noted that this picture is inferred in an earlier work [9] where it is stated that "the first, constant term [corresponding to Z^{ap} in Eq. (22) in the present article] ... corresponds to a process-dependent (valence quark scattering) contribution, whereas the second, logarithmically rising one is universal (gluon scattering). We conclude that it is the Fermi National Accelerator Laboratory (-ISR) energy interval where $\sigma^{\rm MB}/\sigma^{\rm BB}$ (the ratio of the $\sigma_{\rm tot}$ for meson-baryon scattering to the baryon-baryon scattering) comes closest to $2/3$. With the further increase of energy the ratio will approach unity."

In the arguments of the color glass condensate (CGC) of QCD, the gluon component of the target particle drastically increases in high-energy scattering. This is based on the calculation of perturbative QCD. The radius R of the "black" region, where strong absorption of incident particles occurs, increases plausibly by a log$s$ term with a universal coefficient. The $\sigma_{\rm tot}$ may be given by $2\pi R^2$, and the factor B is expected to be universal for πp, Kp and $\bar{p}p$, pp.

In Ref. [6] the s_0 as well as B are taken to be universal in the fittings. The $\sqrt{s_0}$ is not suggested to be process independent in either Ref. [9] or in the framework of CGC. In Table X the values of $\sqrt{s_0}$ for the relevant three processes seem to be closer to each other in the case with the FESR, compared to the case without the FESR. This possibility will be investigated in the next subsection.

F. Analysis with the common value of B

Our analyses in the previous subsections suggest the universality of B in πp, Kp and $\bar{p}(p)p$ scatterings. Now let us try to fit all the data by taking the same value of B from the beginning. The $\sigma_{\rm tot}$ above $k \geq 20$ GeV and ρ above $k \geq 5$ GeV for $\pi^{\mp}p$, $K^{\mp}p$, $\bar{p}(p)p$ scatterings are fitted simultaneously. There are three sets of parameters, c_2, c_1, c_0, $F^{(+)}(0)$, $\beta_{P'}$, β_V. The three FESRs (14), (17), and (20) are used as constraints. Now the three c_2 are not independent. They are represented by one universal B parameter through Eq. (24). So the number of fitting parameters is 13. Successful fits are obtained with the total $\chi^2 = 429.55 = 150.83(\pi^{\mp}p) + 64.28(K^{\mp}p) + 214.44(\bar{p}(p)p)$ with $(N_D - N_P) = (508 - 13)$. It is compared with the best-fitted χ^2 for respective data sets with no universality constraints, which are given in Tables IV, VI, and VIII: $\chi^2/(N_D - N_P) = 150.51/(162 - 5)$ for $\pi^{\mp}p$, $63.80/(111 - 5)$ for $K^{\mp}p$, $214.32/(235 - 5)$ for $\bar{p}(p)p$. Their sum is 428.62. The increase of the total χ^2 is, thus, only 0.93. The constraint of the universal B is consistent with the present experimental data.

The value of B in this universality fit is given by

$$B = 0.285 \pm 0.013 \text{ mb}. \tag{27}$$

The values of $\sqrt{s_0}$ and Z^{ap} are also given in the upper half of Table XI.

By taking the value of B to be universal, the best-fitted values of $\sqrt{s_0}$ become closer to each other. Successful fits are obtained in Ref. [6] by taking both B and s_0 to be universal. We also try to fit the data by taking both B and s_0 as common in the relevant three processes. The resulting $\chi^2 = 435.24 = 152.19(\pi^{\mp}p) + 64.06(K^{\mp}p) + 219.00(\bar{p}(p)p)$ with 11 parameters, and the fit is successful. The total increase of χ^2 is 6.62 from the best fits to the respective processes with no constraints from B and s_0.

The values of the parameters are given in the lower half of Table XI. B and $\sqrt{s_0}$ are given by $B = 0.304 \pm 0.010$ mb and $\sqrt{s_0} = 5.75 \pm 0.34$ GeV. These values are consistent with the results given by PDG [6], $B = 0.308(10)$ mb and $\sqrt{s_0} = 5.38(50)$ GeV, which are obtained by assuming the universality of B and s_0. Another interesting feature is the ratio of Z^{ap}. It satisfies approximately the quark model prediction, $Z^{\pi p}:Z^{Kp}:Z^{pp} = 2:2:3$.

TABLE XI. Values of the best-fit parameters assuming universality of B and of B and s_0, which are taken to be common in fitting the data of relevant processes. The B, Z^{ap}, and $\sqrt{s_0}$ are related with c_2, c_0, and c_1 by Eqs. (24)–(26). The $\beta_{P'}$ are obtained from values of the other parameters through the FESR.

	B (mb)	$\sqrt{s_0}$ (GeV)	Z^{ap} (mb)	$F^{(+)}(0)$	β_V	$\beta_{P'}$
πp	0.285(13)	5.40(37)	21.24(16)	0.13(61)	0.040 12(95)	0.1527(62)
Kp	0.285(13)	5.17(38)	17.91(19)	2.33(1.01)	0.5618(82)	0.4296(481)
$\bar{p}(p)p$	0.285(13)	4.82(49)	35.44(32)	10.41(60)	3.723(36)	6.637(198)
πp	0.304(10)	5.75(34)	21.36(15)	−0.10(61)	0.040 43(93)	0.1472(61)
Kp	0.304(10)	5.75(34)	18.19(16)	2.11(1.01)	0.5613(81)	0.3535(461)
$\bar{p}(p)p$	0.304(10)	5.75(34)	36.04(17)	9.88(53)	3.745(35)	6.232(122)

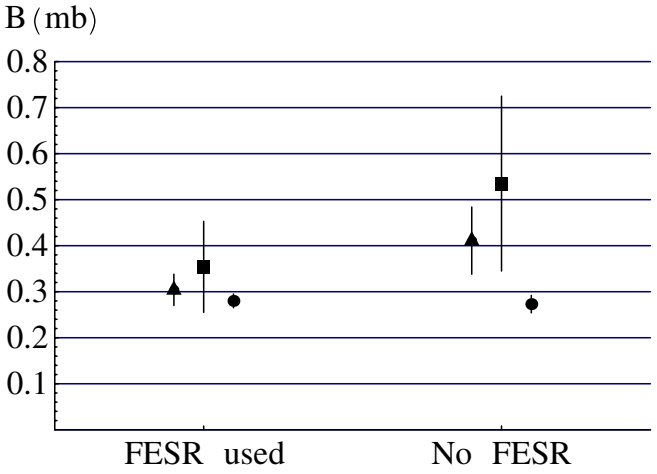

FIG. 12 (color online). Values of the B parameters in Table X: Results without the FESR are on the RHS and ones with the FESR are on the LHS. Triangles, squares, and circles represent $B_{\pi p}$, B_{Kp}, and B_{pp}, respectively. Errors represent 1 standard (1σ) deviations. $B_{\pi p} = B_{Kp} = B_{pp}$ is satisfied within 1σ in the case with the FESR, while we do not obtain any definite conclusion in the case without the FESR.

V. CONCLUDING REMARKS

In order to test the universal rise of the total cross section $\sigma_{\rm tot}^{(+)}$ by $\log^2 s/s_0$ in all the hadron-hadron scatterings, we analyze $\pi^{\mp} p$, $K^{\mp} p$ and $\bar{p}(p)p$ scatterings independently. Rich information of low-energy scattering data constrain, through the FESR, the parameters in the high-energy asymptotic formula to fit the experimental $\sigma_{\rm tot}$ and ρ ratios. The values of the B parameters, the coefficients of the $\log^2 s/s_0$ term in $\sigma_{\rm tot}^{(+)}$, are obtained individually for three processes by these analyses. The results are given in the LHS of Table X, which is explicitly shown in Fig. 12. We obtain

$$B_{\pi p} \simeq B_{Kp} \simeq B_{pp}. \tag{28}$$

The results are consistent with the universality of B within 1 standard deviation. The universality of B is suggested in our analyses.

There are several remarks about our results.

(i) In order to obtain the above conclusion, it is essential to use the FESR as constraints between fitting parameters. As shown in the RHS of Fig. 12, if we do not use the FESR, $B_{\pi p}$ and B_{Kp} cannot be estimated with sufficient accuracy, and we could not obtain any definite conclusion.

(ii) The absolute magnitude of B in the best fit is dependent largely upon the energy region of the fitting in the present $\bar{p}p$ scattering data. In the fit to all the data up to Tevatron energy $\sqrt{s} = 1.8$ TeV, the B_{pp} is estimated as $B_{pp} = 0.280 \pm 0.015$ mb, which predicts the $\sigma_{\rm tot}^{pp} = 108.0 \pm 1.9$ mb at the LHC energy $\sqrt{s} = 14$ TeV. While if only the data up to the ISR energy $\sqrt{s} = 63$ GeV are taken into account, we obtain $B_{pp} = 0.317 \pm 0.034$ mb, which predicts $\sigma_{\rm tot}^{pp} = 113.2 \pm 4.6$ mb at the LHC energy. This value is consistent with the above prediction, but its central value is somewhat larger than our previous result [3,17]. The precise measurement of $\sigma_{\rm tot}^{pp}$ at the LHC [13,14] will help to fix the uncertainty of the absolute magnitude of B.

(iii) Our approach can be checked by the measurement of $\sigma_{\rm tot}^{pp}$ at the LHC. Our predicted values of $\sigma_{\rm tot}^{pp}$ and ρ^{pp} at $\sqrt{s} = 14$ TeV at the LHC, as well as the other predictions [34], are given in Table XII for comparison. The predictions in various models cover a wide range of values. The LHC will select among these approaches.

(iv) The best-fitted values of $B_{\pi p}$ and B_{Kp} are almost the same. This result is important since it suggests that the value of B is independent of quark flavors.

TABLE XII. Predictions of $\sigma_{\rm tot}^{pp}$ and ρ^{pp} at the LHC energy $\sqrt{s} = 14$ TeV in various models.

Reference	$\sigma_{\rm tot}^{pp}$ (mb)	ρ^{pp}
II [this work]	108.0 ± 1.9	0.1312 ± 0.0024
II [3]	$106.3 \pm 5.1_{\rm syst} \pm 2.4_{\rm stat}$	$0.126 \pm 0.007_{\rm syst} \pm 0.004_{\rm stat}$
BH [4]	107.3 ± 1.2	0.132 ± 0.001
BSW [35]	103.6	0.122
GLMM [36,37]	92.1, 110.5	
RMK [38]	91.7	
COMPETE [39]	$111.5 \pm 1.2_{\rm syst}\ ^{+4.1}_{-2.1_{\rm stat}}$	$0.1361 \pm 0.0015_{\rm syst}\ ^{+0.0058}_{-0.0025_{\rm stat}}$
MN [40]	106.4	0.127
GKS [41]	128	0.19
CS [42]	152	0.26
PP [43]	$106.73^{+7.56}_{-8.50}$	$0.1378^{+0.0042}_{-0.0612}$
ILP [44]	110	0.12
Landshoff [45]	125 ± 25	

$B_{\pi p}$ is also consistent with B_{pp}. Thus, we expect the universality of $\sigma_{\text{meson-baryon}} \simeq \sigma_{\text{baryon-baryon}}$, independently of quark flavors at super high energies, as was suggested in Refs. [9–11]. In order to establish the universality of B for all the hadronic scatterings, it is also important to analyze the other processes, such as $\Sigma^- p$ and Λp scatterings.

(v) If the universality of B is established both theoretically and experimentally, the total cross sections of all the hadronic scatterings can be described simply by Eq. (3), $\sigma_{\text{tot}} \simeq B\log^2 s/s_0 + Z^{ap}$, for $\sqrt{s} > \sim\sqrt{s_0} \simeq 5$ GeV, where the effects from the Regge poles of P' and of the vector trajectory become negligible. B is a universal constant. There is an interesting possibility that $\sqrt{s_0}$ is universal. There is no way of predicting values of Z^{ap}, which are highly nonperturbative objects. The difference between $Z^{\pi p}$ and Z^{Kp} is not large, about 3 mb, and $Z^{\pi p}$, Z^{Kp}, and Z^{pp} approximately satisfy the ratio 2:2:3, predicted by the quark model.

[1] K. Igi and M. Ishida, Phys. Rev. D **66**, 034023 (2002).
[2] J. R. Cudell *et al.* (COMPETE Collaboration), Phys. Rev. D **65**, 074024 (2002).
[3] K. Igi and M. Ishida, Phys. Lett. B **622**, 286 (2005).
[4] M. M. Block and F. Halzen, Phys. Rev. D **72**, 036006 (2005); **72**, 039902(E) (2005).
[5] M. Ishida and K. Igi, Phys. Lett. B **670**, 395 (2009).
[6] W.-M. Yao *et al.* (Particle Data Group), J. Phys. G **33**, 337 (2006).
[7] M. Froissart, Phys. Rev. **123**, 1053 (1961).
[8] A. Martin, Nuovo Cimento **42**, 930 (1966).
[9] L. L. Jenkovszky, B. V. Struminsky, and A. N. Wall, Yad. Fiz. **46**, 1519 (1987); Report No. ITP-86-82E, 1986.
[10] E. Ferreiro, E. Iancu, K. Itakura, and L. McLerran, Nucl. Phys. **A710**, 373 (2002).
[11] L. Frankfurt, M. Strikman, and M. Zhalov, Phys. Lett. B **616**, 59 (2005).
[12] E. Iancu, A. Leonidov, and L. McLerran, Nucl. Phys. **A692**, 583 (2001); Phys. Lett. B **510**, 133 (2001).
[13] TOTEM: Technical Design Report No. CERN-LHCC-2004-002 and addendum CERN-LHCC-2004-020.
[14] ALFA, ALFA Detector: Technical Design Report, ATLAS Forward Detectors for Measurement of Elastic Scattering and Luminosity, Report No. ATLAS-TDR-018 and No. CERN-LHCC-2008-004.
[15] U. Dersch *et al.* (SELEX Collaboration), Nucl. Phys. **B579**, 277 (2000).
[16] M. Ishida and K. Igi, Eur. Phys. J. C **52**, 357 (2007).
[17] K. Igi and M. Ishida, Prog. Theor. Phys. **116**, 1097 (2006).
[18] K. Igi, Phys. Rev. Lett. **9**, 76 (1962).
[19] K. Igi and S. Matsuda, Phys. Rev. Lett. **18**, 625 (1967).
[20] R. Dolen, D. Horn, and C. Schmid, Phys. Rev. **166**, 1768 (1968).
[21] F. J. Gilman, H. Harari, and Y. Zarmi, Phys. Rev. Lett. **21**, 323 (1968).
[22] On p. 337 of Ref. [6] $\sigma_{\text{tot}}^{\bar{a}p,ap}$ is given by $\sigma_{\text{tot}}^{\bar{a}p,ap} = Z^{ap} + B\log^2\frac{s}{s_0} + Y_1^{ap}(\frac{s_1}{s})^{\eta_1} \pm Y_2^{ap}(\frac{s_1}{s})^{\eta_2}$. The scale s_1 is fixed to be 1 GeV^2. The $(B, \sqrt{s_0}, \eta_1, \eta_2) = (0.308(10)$ mb, 5.38(50) GeV, 0.458(17), 0.545(7)) was obtained process independently. The process-dependent parameters $(Z^{ap}, Y_1^{ap}, Y_2^{ap})$ are obtained as (20.86(40), 19.24(1.22), 6.03(19)), (17.91(36), 7.1(1.5), 13.45(40)) and (35.45(48), 42.53(1.35), 33.34(1.04)) for $\pi^{\mp}p$, $K^{\mp}p$ and $\bar{p}(p)p$, respectively. We obtained $\text{Im}f_{\text{PDG}}^{\bar{a}p,ap}(\nu)$ by $\frac{k}{4\pi} \times \sigma_{\text{tot}}^{\bar{a}p,ap}$ with the central values of these parameters. Multiplying $\text{Im}f_{\text{PDG}}^{\bar{a}p,ap}(\nu)$ with the $\rho^{\bar{a}p,ap}$ data at the corresponding energies, we obtained the data for $\text{Re}f^{\bar{a}p,ap}$. Here we omit errors of $\sigma_{\text{tot}}^{\bar{a}p,ap}$ since errors of $\rho^{\bar{a}p,ap}$ are generally larger than $\sigma_{\text{tot}}^{\bar{a}p,ap}$.
[23] M. M. Block, Nucl. Instrum. Methods Phys. Res., Sect. A **556**, 308 (2006).
[24] The following data points are removed: $(k(\text{GeV}), \sigma_{\text{tot}}^{\bar{p}p}(\text{mb})) = (2.5, 79.4 \pm 1.0)$, $(3.54, 69.7 \pm 0.5)$, $(3.6, 76.2 \pm 1.8)$, $(4.0, 71.0 \pm 1.0)$, $(4.015, 66.84 \pm 0.32)$, $(4.3, 60.6 \pm 0.8)$, $(9.14, 57.51 \pm 0.73)$. This procedure is explained in Ref. [17].
[25] $\chi^2 = 48.8$ for sieved $\bar{p}p$ data includes the factor $R = 1.140$. See Ref. [23].
[26] We adopt a different treatment of data from Ref. [5], where systematic errors were taken to be larger than those in the original ones [6].
[27] N. A. Amos *et al.* (E710 Collaboration), Phys. Rev. Lett. **68**, 2433 (1992).
[28] C. Avila *et al.* (E811 Collaboration), Phys. Lett. B **445**, 419 (1999).
[29] F. Abe *et al.* (CDF Collaboration), Phys. Rev. D **50**, 5550 (1994).
[30] The original data of ρ^{pp} give no successful fits, since the data are mutually inconsistent with different experiments. Data points from Refs. [31,32] have comparatively small errors, and seem to be inconsistent with the other data sets upon inspection. We have tried to fit the data set only including [31] for ρ^{pp} in the relevant energy region, but it is not successful. We remove these two data sets from our best fit.
[31] L. A. Fajardo *et al.*, Phys. Rev. D **24**, 46 (1981).
[32] G. Bellettini *et al.*, Phys. Lett. **14**, 164 (1965).
[33] Reference [6] treats the scatterings of $\bar{p}(p)p$, $\bar{p}(p)n$, $\Sigma^- p$, $\pi^{\mp}p$, $K^{\mp}p$, $K^{\mp}n$, γp, $\gamma\gamma$. All data sets are fitted by using a common value of B (and a common value of s_0). The resulting B is $B = 0.308(10)$ mb.
[34] R. Fiore, L. Jenkovszky, R. Orava, E. Predazzi, A. Prokudin, and O. Selyugin, arXiv:0810.2902v2.
[35] C. Bourrely, J. Soffer, and T. T. Wu, Nucl. Phys. **B247**, 15

(1984).
[36] E. Gotsman, E. Levin, U. Maor, and J. S. Miller, Eur. Phys. J. C **57**, 689 (2008).
[37] E. Gotsman, E. Levin, and U. Maor, arXiv:0708.1506.
[38] M. G. Ryskin, A. O. Martin, and V. A. Khoze, Eur. Phys. J. C **60**, 249 (2009).
[39] J. R. Cudell *et al.* (COMPETE Collaboration), Phys. Rev. Lett. **89**, 201801 (2002).
[40] E. Martynov and B. Nicolescu, Eur. Phys. J. C **56**, 57 (2008).
[41] S. V. Goloskokov, S. P. Kuleshov, and O. V. Selyugin, Z. Phys. C **50**, 455 (1991).
[42] J. R. Cudell and O. V. Selyugin, Phys. Lett. B **662**, 417 (2008).
[43] V. A. Petrov and A. Prokudin, Eur. Phys. J. C **23**, 135 (2002).
[44] M. M. Islam, R. J. Luddy, and A. V. Prokudin, Phys. Lett. B **605**, 115 (2005).
[45] P. V. Landshoff, Acta Phys. Pol. B **39**, 2063 (2008).